

Dissipationless Flow and Superfluidity in Gaseous Bose-Einstein Condensates

C. Raman,* R. Onofrio, J. M. Vogels, J. R. Abo-Shaeer, and W. Ketterle

*Department of Physics and Research Laboratory of Electronics,
Massachusetts Institute of Technology, Cambridge, Massachusetts 02139*

(Received August 21, 2000; accepted October 16, 2000)

We study dissipation in a dilute Bose gas induced by the motion of a macroscopic object. A blue-detuned laser beam focused on the center of a trapped gas of sodium atoms was scanned both above and below the BEC transition temperature. The measurements allow for a comparison between the heating rates for the superfluid and normal gas.

1. INTRODUCTION

Superfluid flow is a manifestation of quantum mechanics at the macroscopic level. Phenomena like dissipationless flow and persistent currents can be traced back to the existence of a macroscopic wavefunction. The gradient of its phase gives the superfluid velocity¹. However, superfluid flow is only stable below a critical velocity. Above this velocity, excitations of the fluid can be generated, which can be either phonons, rotons (in liquid ⁴He) or vortices.

The realization of Bose-Einstein condensation in dilute gases^{2,3} has created a new test ground for the theory of quantum fluids. Early experiments confirmed the microscopic foundation of the phenomenon of superfluidity: the phonon nature of low-lying collective excitations was observed⁴⁻⁶ and the coherence or macroscopic phase of the condensate.⁷ This picture became more complete during the last year with the observation of vortices,^{8,9} transverse excitations,¹⁰ evidence for a critical velocity¹¹ and suppression of collisions.¹² Although the metastability and therefore limited lifetime of the quantum gas and its mesoscopic size may prevent spectacular observations of persistent flows, there is already a clear picture emerging of the many facets of superfluidity in a gas.

*E-mail: craman@mit.edu

In this article we present measurements which indicate a regime of frictionless flow for a gaseous Bose-Einstein condensate. We emulate the motion of a macroscopic object by scanning a focused, blue-detuned laser beam through the gas at different velocities. By taking measurements on nearly pure condensates as well as purely thermal ensembles, we can compare the relative role of dissipation in both phases. This extends our previous work^{11, 13} where we studied dissipation in a Bose condensed system.

2. THE EXPERIMENTAL SET-UP

The experiments were performed in a new apparatus for the production of Bose-Einstein condensates of sodium atoms. The apparatus has been functioning since January 1999 and incorporates some improvements with respect to the original machine of the MIT group. In particular, a Zeeman slower with magnetic field reversal (“spin-flip” Zeeman slower) delivered a flux of typically 10^{11} atoms s^{-1} . This resulted in trapping $2 - 3 \times 10^{10}$ atoms in a dark-spontaneous force optical trap at a temperature of $\simeq 1$ mK. After 3–4 ms of polarization gradient cooling, atoms at a temperature of 50–100 μ K were loaded into an Ioffe-Pritchard magnetic trap. The trap consisted of four Ioffe bars and two elongated pinch coils, symmetrically located around a quartz cell, combining tight confinement and excellent optical access on four sides of the glass cell. Under the tightest confinement, the cylindrically symmetric confining potential has radial and axial trapping frequencies $\nu_r = 547$ Hz and $\nu_z = 26$ Hz. The initial stage of evaporative cooling (18 s) proceeded using this trapping configuration; however, the final stage evaporation appeared to be limited by inelastic losses at high densities. Therefore, the magnetic confinement was reduced in the last 5–7 s, finally producing condensates of $2-5 \times 10^7$ atoms in traps of radial frequencies $\nu_r = 40-80$ Hz and axial frequency $\nu_z = 20$ Hz. Since decompression occurred during the evaporation and not after the condensate is produced as in previous work,¹¹ non-adiabatic effects which lead to heating were eliminated. Thus nearly pure condensates (>90% condensate fraction) were produced regardless of the final trapping geometry.

A 514 nm laser beam used to stir the atoms was split off from the argon-ion laser that pumped the dye laser used for the cooling and trapping beams. Such focused blue-detuned beams have been used previously to eliminate Majorana losses in the center of a quadrupole magnetic trap¹⁴ and to excite sound waves.⁶ A single mode optical fiber significantly improved the stability with respect to previous experiments.¹¹ The position of the laser focus did not change by more than a few μ m per day and required only minimal adjustment to keep it centered on the atomic cloud. The laser was focused to a Gaussian $1/e^2$ beam diameter of 10 to 13 μ m.

The repulsive optical dipole force expelled the atoms from the regions of highest laser intensity, and we typically used a ratio of barrier height to chemical potential (or temperature, in the case of purely thermal clouds) of 5–10. The condensate had a mean-field energy of 60–140 nK, while the thermal cloud temperature was varied between 1 and 6 μ K. Thus, about 200–400 μ W of laser power were required for stirring a condensate, and 6–10 mW for stirring a thermal cloud.

The laser was focused on the center of the cloud by observing the “pierced” condensate using in-situ phase-contrast imaging.¹³ The focus was scanned back and forth along the axial direction using an acousto-optic deflector. The velocity of the scan was varied by adjusting the frequency f and keeping the amplitude α fixed, yielding a velocity of $v = 2\alpha f$. The scan amplitude was chosen to be between a few beam diameters and an amplitude of one-half the diameter of the cloud, about 80 μ m. For thermal clouds, we typically scanned the full diameter of the cloud. A schematic of the experimental set-up, including the imaging system, is depicted in Fig. 1.

3. ENERGY DISSIPATION IN BOSE-EINSTEIN CONDENSATES

Exposing a Bose condensate to the stirring laser beam transferred energy to the atoms, resulting (after equilibration) in an increase in the thermal component. We measured this component by turning off the scan, allowing the gas to equilibrate for 100–200 ms and then shutting off the magnetic trap. After ballistic expansion for a fixed time, typically 50 ms, the atoms were exposed to a $\sim 500 \mu$ s pulse of near-resonant light, and the shadow cast by the atoms was imaged onto a CCD camera. The two-dimensional transmission profile yielded the column density of the cloud and the kinetic energy distribution of the atoms. For mixed clouds this distribution was bimodal, with the condensate localized in the center and the more dilute thermal component appearing in the wings. Our technique allowed us to measure energy changes as little as 10 nK, in a regime where the thermal fraction ($< 10\%$) was barely visible in the images.

We employed this technique in earlier work to analyze the heating induced by stirring the condensate with a blue-detuned laser beam at various velocities.¹¹ There the temperature increase suggested two regimes of dissipation separated by a velocity threshold. However, a precise determination of the critical velocity was not possible since the sensitivity of the measurements was limited by fluctuations in the background heating processes such as inelastic collisions. As a result, the small heating rate due to the stirrer near the critical velocity, of the order of 20 nK/s, could not be detected. Moreover, the initial thermal fraction could not be suppressed below 40% due to non-adiabatic effects during decompression of the magnetic trap.

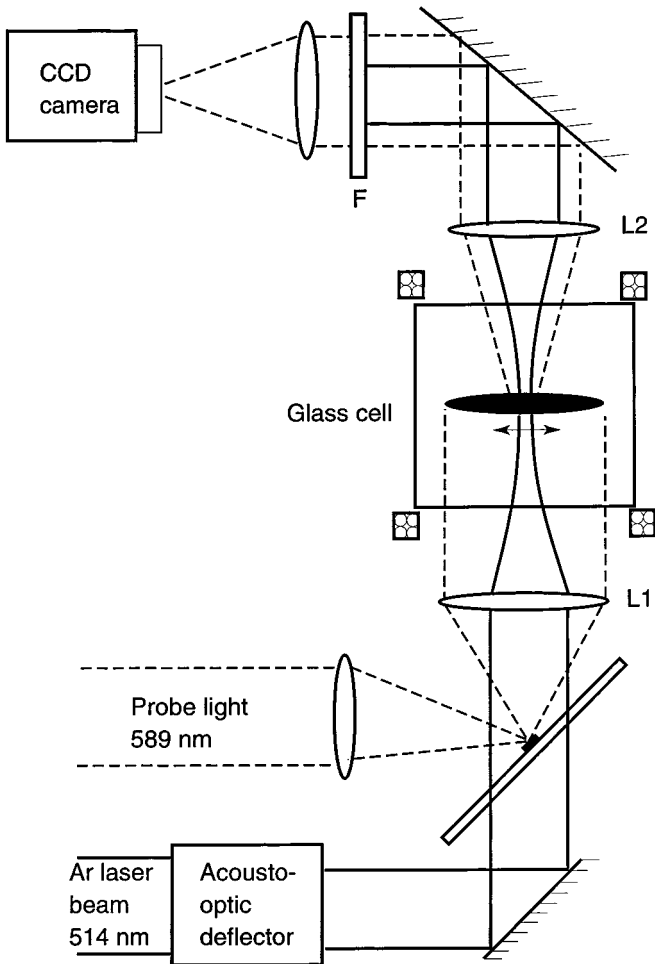


Fig. 1. Schematic view of the experimental setup. The condensate was confined in a glass cell using an Ioffe-Pritchard magnetic trap. The blue-detuned laser beam was sent through a two-axis AOM scanner and then focused on the condensate using the Lens L1. The probe light was overlapped using a small mirror and, after passing through the condensate, was focused with the lens L2 and sent to the CCD camera. The filter F was used to avoid exposure of the CCD camera to the high intensity blue-detuned laser beam.

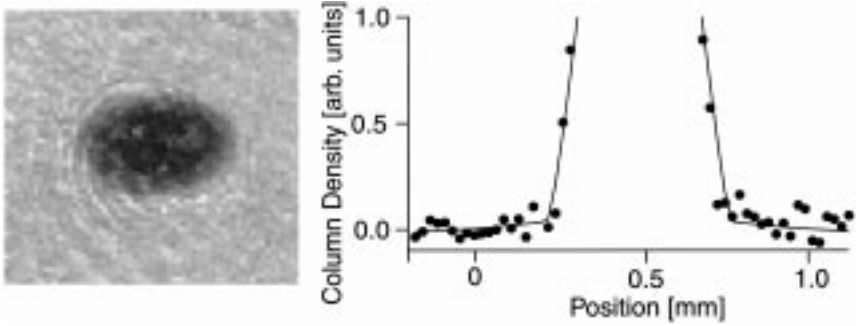


Fig. 2. High sensitivity calorimetry. Shown is an absorption image of an expanded cloud. On the right is a one-dimensional vertical slice taken through the center of the image which represents the column density $\tilde{n} = -\ln T$, where T is the transmission of the probe light. The vertical axis is expanded to see the extremely dilute thermal wings. The solid line is a constrained two-dimensional bimodal fit, which yields a thermal fraction of $(6 \pm 0.6)\%$.

By optimizing the evaporation strategy, we have achieved nearly pure ($>90\%$) condensates as initial conditions for the stirring experiments. While background heating processes could not be fully eliminated, we could account for them by subtracting the energy of stirred and unstirred clouds. Thus, even with a nearly invisible thermal component we can detect changes in the non-condensed fraction of a few percent. Using this method, we have measured the small heating present near the critical velocity that was previously indiscernible.

Figure 2 shows a normalized image of the probe light transmitted by the atomic cloud. The data can be described by a bimodal velocity distribution comprised of a Thomas-Fermi profile for the condensate and a Gaussian distribution for the thermal component,²

$$\tilde{n}(\rho, z) = \tilde{n}_C \left(1 - \frac{\rho^2}{\rho_C^2} - \frac{z^2}{z_T^2}\right)^{3/2} + \frac{\tilde{n}_T}{g_2(1)} g_2(e^{-(\rho^2/\rho_T^2 + z^2/z_T^2)}) \quad (1)$$

where ρ and z are the radial and axial directions, respectively, ρ_C and ρ_T the radial size of condensate (Thomas-Fermi radius) and thermal component, respectively, and z_C and z_T the same for the axial sizes. \tilde{n}_C and \tilde{n}_T are the peak column density of the condensate and thermal cloud in the time-of-flight absorption image. The Bose function is $g_n(x) = \sum_{k=1}^{\infty} x^k/k^n$.

The temperature of the thermal cloud is determined from the width of the Gaussian distribution,

$$k_B T = \frac{1}{2} M z_T^2 \left(\frac{\omega_z^2}{1 + \omega_z^2 t^2} \right) \simeq \frac{1}{2} M \frac{z_T^2}{t^2} \quad (2)$$

where the latter approximation holds for long time of flight $\omega_z t \gg 1$. The number of thermal atoms is $N_T = \int \tilde{n}_T(\rho, z) dz = \pi [g_3(1)/g_2(1)] \tilde{n}_T \rho_T z_T \simeq 2.3 \tilde{n}_T \rho_T z_T$. Due to the high optical density in the center of the images, the number of condensate atoms was more reliably extracted from the mean-field energy μ rather than the integrated column density. In the Thomas-Fermi limit this is $\mu = \frac{1}{2}(15\bar{\omega}^3 \hbar^2 \sqrt{M N_C a})^{2/5}$, where $\bar{\omega} = (\omega_r^2 \omega_z)^{1/3}$ is the mean angular trapping frequency, and $a = 2.75$ nm is the two-body scattering length for sodium. Equating mean-field energy to the measured kinetic energy we get $\mu = \frac{1}{2}M(\rho_C^2 + \frac{1}{2}z_C^2)/t^2$, where t is the time-of-flight. The total number is $N = N_T + N_C$.

The transmitted fraction of the probe light was determined by the ratio of images taken with and without the atoms present. The two-dimensional data were fitted to the function $f(\rho, z) = C e^{-\sigma \bar{n}(\rho, z)}$, where σ is the known absorption cross-section. In general, one can fit all of the unknown parameters N_T/N , N_C/N , N , ρ_T , z_T , ρ_C , z_C , as well as the rotation angle of the image in the ρ - z plane and a scale factor C caused by fluctuations in the probe light intensity between the two images.

For very low temperatures the spatial extent ρ_T, z_T of the thermal component as well as its column density \tilde{n}_T diminish considerably. It became very difficult to reliably extract thermal fractions below 10% from an unconstrained bimodal fit of the form given in Eq. 1. Therefore, we constrained the thermal fit parameters N_T/N , ρ_T and z_T to reflect the correlation between the number of thermally excited atoms and the temperature, a relationship which may be parameterized in different ways. For example, for an ideal Bose gas, the thermal fraction and energy per particle are

$$\left. \frac{N_T}{N} \right|_0 = \left(\frac{T}{T_c} \right)^3 \quad (3)$$

$$\left. \frac{E}{Nk_B T_c} \right|_0 = \frac{3g_4(1)}{g_3(1)} \left(\frac{T}{T_c} \right)^4 \quad (4)$$

where T_c is the transition temperature. Including the effect of the finite mean-field energy μ increases the thermal fraction (and therefore the total energy), yielding a correction to the above expressions

$$\frac{N_T}{N} = \left. \frac{N_T}{N} \right|_0 + \xi(T/T_c, \eta) \quad (5)$$

$$\frac{E}{Nk_B T_c} = \left. \frac{E}{Nk_B T_c} \right|_0 + \tau(T/T_c, \eta) \quad (6)$$

where $\eta = \mu_{T=0}/k_B T_c$. We parameterized the functions ξ and τ which had been numerically evaluated for specific values of η in the range 0.3–0.45 using mean-field theory, neglecting interactions within the thermal cloud.¹⁵ The approximation implied in this model has been used to successfully predict static thermodynamic properties and low-temperature collective excitations in dilute Bose gases.¹⁶ This approach is valid for our experimental conditions, where the thermal atoms are extremely dilute and few in number. By inverting Eq. (5) we obtain for the total energy of the gas

$$\frac{E}{Nk_B T_c} = \varepsilon(N_T/N, \eta) \quad (7)$$

where the function ε is determined by the functions ξ and τ . The parameters n_T , ρ_T , and z_T can now be expressed in terms of a single parameter, the thermal fraction N_T/N . Without this constraint, the fitting routine tended to increase the spatial extent ρ_T , z_T of the thermal cloud when the column density \tilde{n}_T is low, an unphysical result.

By imposing this constraint we could extend the bimodal fitting technique to temperatures close to the chemical potential μ . Figure 2 shows a one-dimensional vertical slice taken through the image data, converted into column density of the cloud. The thermal wings appear at about 0.3 mm from the center of the image, near the edge of the condensate. Although the thermal cloud is extremely dilute, the constrained fitting routine has no difficulty detecting the 6% normal fraction of the gas present in the image. With this technique, the energy per particle of the gas can be established with an uncertainty of about 10 nK, for temperatures as low as $k_B T/\mu = 1.2$. To our knowledge, this combination of high sensitivity and low temperature thermometry has not been previously reported.

Figure 3 shows the heating of the condensate versus the velocity of the laser beam. The velocity was varied by changing the frequency of the laser beam while keeping the scan amplitude fixed at roughly 1/3 of the axial Thomas-Fermi diameter. The heating rate was measured by adjusting the stirring time between 30 ms and 8 s while keeping the total energy transfer roughly the same for all velocities used. Earlier data taken by varying the amplitude while keeping the frequency fixed at 56 Hz, about 3 times the axial trapping frequency,¹¹ are shown for comparison. The peak sound velocity is about 6 mm/s for both old and new data. The absolute scaling of the ordinate depends on our exact knowledge of the number of condensate atoms, which may have an uncertainty of up to a factor of 2. However, since the same method was applied to all data points, the error bars represent a fair measure of the significance of features present in the new data. Moreover, the overall similarity of the two data sets is remarkable, given

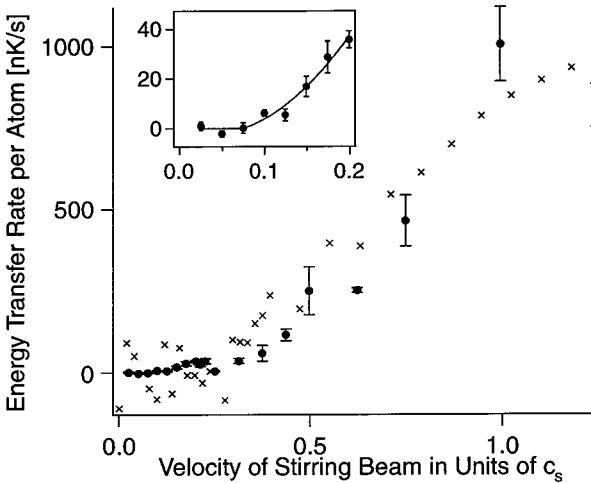


Fig. 3. Calorimetry of a condensate. Shown is the energy transfer rate versus velocity of the stirring laser beam measured using subtraction of background heating processes (full circles) and older data taken from ref. 11 without background subtraction (crosses). The velocity is in units of the peak sound velocity in the condensate, 5.9 mm/s and 6.2 mm/s, for the new and old data, respectively. The error bars reflect shot-to-shot variations in the temperature, which is the largest source of error. The inset is a magnification of the region near zero velocity, showing sensitivity to ~ 20 nK/s heating rates.

the difference in experimental conditions (trapping geometry, thermal fraction, etc.) underlying them.

The new data show a substantial improvement in signal-to-noise with respect to the older set. This enhanced sensitivity allows for a clear resolution of the small heating rate ($\simeq 20$ nK/s) visible at low velocities near $v/c_s \simeq 0.15$. This is shown in the inset, which is a magnified plot of the data in the low velocity region. These data suggest that the critical velocity for excitation occurs at $v_c \simeq 0.1c_s$, as confirmed by direct measurements of the drag force from the asymmetry of the condensate density profile induced by the scanning laser beam.¹³ This technique was shown to be consistent with the calorimetric measurements, but had a higher sensitivity at low velocities.

Above the critical velocity the condensate experiences a drag force. We assume that close to v_c the drag force increases linearly with velocity, i.e., $F = \kappa(v - v_c)$, where κ is the coefficient of drag. Such a relation was derived by several authors for $T = 0$ condensates.^{17, 18} The rate of energy transfer is then $F \cdot v$, yielding

$$\frac{dE}{dt} = \kappa v(v - v_c) \quad (8)$$

We can estimate a critical velocity from our data using a parabolic fit above v_c , as suggested by Eq. (8).

Equation (8) yields a critical velocity of $v_c/c_s = 0.07 \pm 0.01$ for the new data. This new value is smaller than estimated in our earlier paper.¹¹ Both experiments are consistent, since the scatter in the observed heating rates in Ref. 11 prevented a clear observation of the threshold, and the critical velocity was estimated by linear extrapolation from high heating rates to be $v_c/c_s = 0.25$. Other possible extrapolations tend to lower the value of v_c , for instance a function $\propto v(v - v_c)$ as suggested by Eq. (8), yielded $v_c/c_s = 0.20 \pm 0.07$ for the data of Ref. 11. With our improved calorimetry we have done measurements using the fixed frequency/variable amplitude method employed earlier and observed a small heating rate of 20 nK/s at $v = 0.15c_s$ that was previously indiscernible. Furthermore, small differences in the laser beam profile, in conjunction with the inhomogeneous nature of the gas, may have also contributed to the higher value of v_c in Ref. 11.

Both data sets show good agreement in the overall heating rate. For the new data above $v/c_s \simeq 0.1$ the heating rate increases, until about 0.2, where it appears to level off and then to drop to a minimum at around $v/c_s \simeq 0.25$. For higher velocities the heating rate increases once again. The suppression of the heating occurring at $v/c_s \simeq 0.25$ arises from a frequency dependent feature, as discussed in Ref. 13. At that velocity the laser scans near the axial trapping frequency and excites synchronous dipole motion of the condensate. This results in a lower relative velocity between condensate and stirrer, thereby reducing the heating.

4. ENERGY DISSIPATION IN A NORMAL GAS

At finite temperature, one would expect heating even below the critical velocity due to physical processes occurring within the normal component. For a dilute Bose gas at temperatures below $0.45T_c$, the thermal fraction is less than 10%, and plays a very minor role in the heating discussed so far. In addition, the repulsive mean field of the condensate lowers the density of the normal component in the center of the cloud even further. This allowed us to study the breakdown of superfluidity due to processes initiated primarily within the condensate, and to neglect interactions between the condensate and thermal component.

There is a major difference in the description of the condensate and the normal component. Interactions within the condensate give rise to quantum fluid properties. The macroscopic wavefunction $\Psi = \sqrt{n} e^{i\phi}$ yields hydrodynamic equations of motion for this fluid, expressed in terms of the density n and superfluid velocity $\mathbf{v} = (\hbar/m) \nabla\phi$. In contrast, a dilute normal gas interacts very weakly with itself and with the condensate. For the most

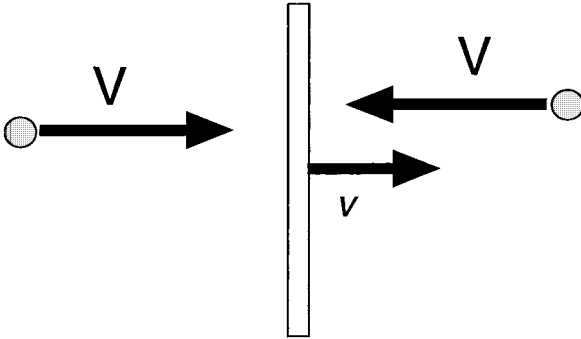


Fig. 4. One-dimensional model for the heating of a thermal cloud. Atoms from both sides collide at velocity V with a wall moving at velocity v .

part, the mean free path for collisions $l_{\text{mfp}} > d$, where d is some characteristic length scale, for example, the laser beam diameter or the radius of the cloud. In this collisionless regime, no correlations between particles exist, and a fluid description in terms of a local density n and a local velocity \mathbf{v} does not hold. However, heating still occurs as long as the thermal atoms collide with the moving laser beam. We present measurements of this heating mechanism in a gas above the transition temperature, which we can understand using a kinetic model. These measurements allow us to compare the relative effectiveness of heating the normal and superfluid components.

Let us first consider a one-dimensional model of a hard wall moving at a velocity v through a gas of atoms with thermal velocity $V \sim \sqrt{2k_B T/M}$ (see Fig. 4). We assume $v \ll V$ and elastic collisions between the atoms and the wall.

An atom moving in the direction of the wall slows down during the collision, while an atom moving against the wall increases its velocity. This leads to a net heating rate due to the finite velocity v . The energy transferred to atoms on the left and right is

$$\Delta E_{\text{left}} = \frac{1}{2}M(-V + 2v)^2 - \frac{1}{2}MV^2 = 2Mv(v - V) \quad (9)$$

$$\Delta E_{\text{right}} = \frac{1}{2}M(V + 2v)^2 - \frac{1}{2}MV^2 = 2Mv(v + V) \quad (10)$$

while the corresponding collision rates are

$$\Gamma_{\text{left}} = nA(V - v) \quad (11)$$

$$\Gamma_{\text{right}} = nA(V + v) \quad (12)$$

where n is the atomic density and A the surface area of the moving wall. The rate of energy increase is therefore

$$\frac{dE}{dt} = \Gamma_{\text{left}} \Delta E_{\text{left}} + \Gamma_{\text{right}} \Delta E_{\text{right}} = 8MnAVv^2 \quad (13)$$

which can be simply interpreted as an energy transfer per collision, $\propto Mv^2$, multiplied by the collision rate nAV . The model is easily extended to three dimensions and objects of arbitrary shapes. We approximate the stirring laser as an infinite cylinder of diameter d moving transversely to its axis of symmetry, along the axial direction of the cylindrically symmetric trap. The frequencies of oscillation along the axial and radial direction are ω_z and ω_r , respectively, and the cloud $1/e^2$ radii are $R_{r,z} = \sqrt{2k_B T / M\omega_{r,z}^2}$. Summing over the Boltzmann velocity distribution, and accounting for the three-dimensional nature of the collisions, the energy transfer rate per particle is:

$$\left. \frac{dE}{dt} \right|_N = 2\pi\eta_A v_z Mv^2, \quad (14)$$

where the geometrical overlap factor $\eta_A = A_b/S = 2d/\pi R_r$ is the ratio between the cross-sectional area of the laser beam, A_b , and that of the thermal cloud, $S = \pi R_r^2$.

Equation (14) has a simple interpretation: each atom moves back and forth in the axial direction at a rate v_z , and within each trapping period a fraction η_A of them hit the stirring beam acquiring an energy $\propto Mv^2$. Figure 5 shows the energy transfer rate to a gas of atoms slightly above the transition temperature, obtained using the calorimetric technique described earlier. We varied the velocity by keeping the scan amplitude fixed to approximately the diameter of the thermal cloud, and varying the scan frequency. The temperature was obtained from a fit to the wings of the cloud.²

To compare with the model calculations Eq. (14) was evaluated for the average of initial and final temperatures (the temperature increased by about a factor of 2 during the stirring) using the experimental parameters $d = 10 \mu\text{m}$, laser power 18 mW, $v_z = 20$ Hz. The laser power was chosen to give a barrier height $U \approx 6k_B T$, where T is the gas temperature. The data clearly show the v^2 dependence on the laser beam velocity up to the thermal velocity $V = \sqrt{2k_B T/M} = 40$ mm/s, as predicted from Eq. (14), thus verifying the basic tenets of the kinetic model of heating. For velocities of the stirrer exceeding the thermal velocity, i.e., $v \gg V$, only atoms moving opposite to the direction of the stirrer can collide with it. Here the heating rate should cross over to a v^3 dependence, although with a different prefactor. Extending the technique presented here to higher velocities might show this effect.

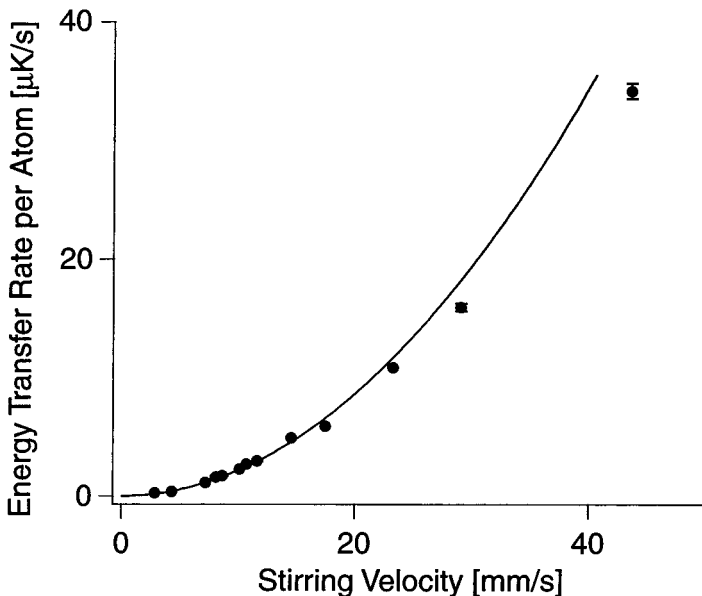


Fig. 5. Heating of the normal gas. The energy transfer rate per particle versus velocity of the moving laser beam is compared to the result of the kinetic model described in the text (solid line).

The observed absolute heating rate also agreed well with the prediction given by Eq. (14) to within 20–30%. The major uncertainty came from the laser beam size, which may have had a 20–30% variability from run to run. In Fig. 6 we show the heating rate for a cloud near $0.78 \mu\text{K}$, plotted versus the ratio of barrier height U_0 to temperature $k_B \bar{T}$, where \bar{T} is the average of initial and final temperatures. In this regime, the heating rate increased in proportion to the effective laser beam size, which scales as $\sqrt{\ln(U_0/k_B \bar{T})}$. The solid line is a fit to this functional form. At higher laser power the data deviate from this fit probably due to additional heating from the non-Gaussian wings of the laser beam.

In the above model, the temperature of the gas only appears through the factor η_A . Therefore, at higher temperatures, where the cloud is more spatially extended, one expects the heating rate to decrease as the size R_r increases, or $dE/dt|_N = \kappa v^2$, where $\kappa \propto d/\sqrt{T}$. We keep the ratio of barrier height to temperature, and therefore the effective laser beam size d , approximately constant. Figure 7 shows the coefficient of heating κ measured for two different stirring velocities v below the thermal velocity, along with the model prediction. The data show decreasing efficiency of

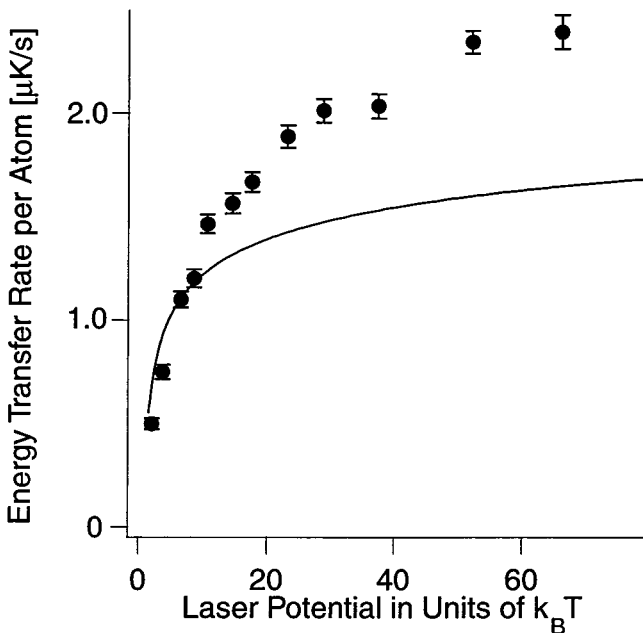


Fig. 6. Dependence of the heating on the power of the stirring laser beam. Shown is the heating of a thermal cloud close to the BEC transition temperature versus the laser beam potential U_0 in units of the temperature $k_B T$. Data were taken by varying the laser power at a fixed stirring velocity of 7 mm/s. The solid line is a fit to the data at low laser power $U \leq 10k_B T$.

heating at high temperatures, which we attribute to the decrease of geometrical overlap between the cloud and the laser beam.

One may ask if the heating measured depends strictly on velocity, or if there is an additional dependence on the scan frequency. For low scan frequencies $f < 20\nu_z$, we observed no difference in the heating for different frequencies at the same laser beam velocity, taking care to avoid the trap resonance at $f = \nu_z = 20.1$ Hz. However, at very high scan frequencies $f \geq 50\nu_z$, the back-and-forth motion of the optical potential becomes time-averaged and appears as a quasi-static perturbation to the atoms. Therefore the heating rate diminished, as seen in Fig. 8, where the heating rate was measured at a fixed scan amplitude and variable frequency.

5. DISCUSSION

Since our first report on critical velocities in a condensate, several theoretical papers have added further insight.^{19–24} The observed critical

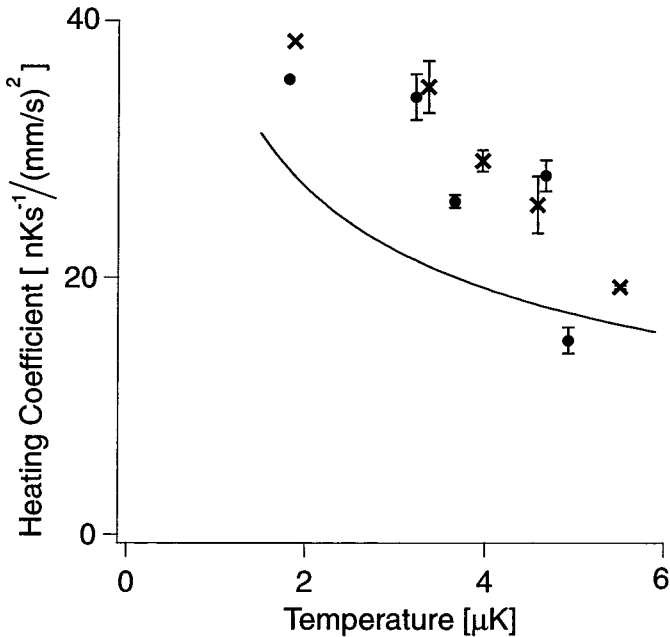


Fig. 7. Temperature dependence of the heating. Plotted is the heating coefficient κ described in the text, for two different velocities, 9.7 mm/s (\times) and 19.4 mm/s (\bullet), versus the average temperature of the gas. The solid line is the value predicted by Eq. (14). The decrease in heating efficiency versus temperature indicates decreasing overlap between the stirrer and the gas.

velocity $v_c \simeq 0.1c_s$ is lower than the predictions for homogeneous^{17, 25} and inhomogeneous²⁶ 2D systems. This discrepancy is most likely due to the actual 3D geometry, where the laser beam pierced lower density regions of the condensate. It was noted in Ref. 22 that the critical velocity for phonon excitation is lowered by the inhomogeneous density distribution. Vortex stretching and half-ring vortices can lower the 3D critical velocity below the 2D value.²⁰ Jackson *et al.*^{19, 24} performed 3D simulations obtaining a critical velocity as low as $0.13c_s$, quite close to our results.

The relevant critical velocity is likely related to the formation of vortices, as numerical simulations have shown.^{17, 19, 24} Vortices form when they are energetically favorable, as expressed by a Landau-type criterion,^{27, 21, 23} and when there is a mechanism to nucleate them. Generally, the latter condition is more stringent, requiring higher velocities of the stirrer for the onset of dissipation. However, for typical conditions of experiments with dilute Bose gases, these two requirements are satisfied within a narrow range of velocities but can be distinguished by the dependence on condensate size

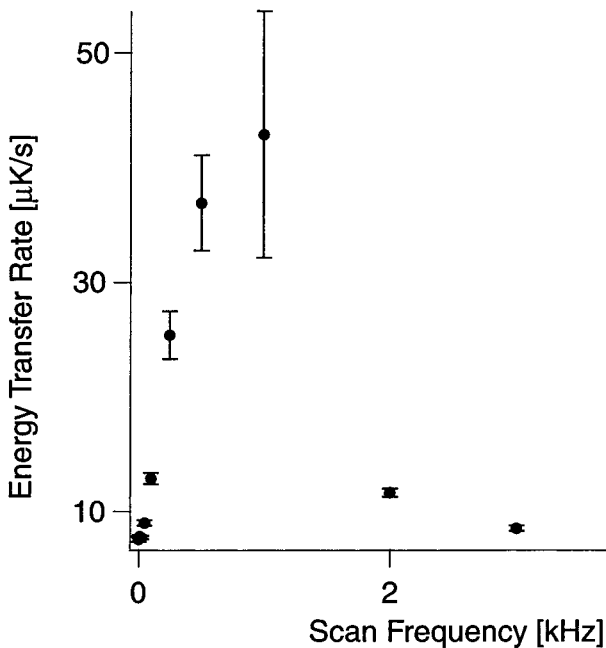


Fig. 8. Heating of a thermal cloud close to the BEC transition temperature versus stirring frequency. The data at low frequency show the velocity dependence of the heating, as seen earlier in the data of Fig. 5. For the frequencies above 1 kHz, the heating rate diminishes due to the time-averaging effect described in the text.

and density. The density dependence of our recent drag force measurements suggest that vortex nucleation plays a dominant role.¹³ However, more extensive measurements on size and density dependence, along with theoretical simulations of the experimental geometry are necessary to identify which processes contribute to the nucleation of vortices.

Alkali gas Bose condensates are an ideal system to study the nucleation of vortices since the wall-free confinement in atom traps provides controlled boundary conditions. This is in contrast to liquid helium where there is usually vorticity present at the surface and nucleation studies are more difficult.

There are differences between a constantly moving object and our scanning laser beam. The rapid turnaround of the laser beam occurring twice per cycle can emit phonons causing additional heating.^{19, 24} This heating should scale with v^2f , where v is the velocity of the scan and f the scan frequency. Our new high sensitivity measurement technique could be used to explore this heating mechanism.

We may compare the superfluid heating with that of the normal gas. Clearly, different mechanisms have been outlined for the thermal cloud and for the condensate. For a thermal gas, the heating rate is

$$\left. \frac{dE}{dt} \right|_T = N_T \kappa_T v^2 \quad (15)$$

while the condensate heating rate above the critical velocity is

$$\left. \frac{dE}{dt} \right|_C = N_C \kappa_C v(v - v_c) \approx N_C \kappa_C v^2 \quad (16)$$

where the approximation holds for $v \gg v_c$. In general we may write the heating rate as $\Delta \cdot \Gamma$, where Δ is the energy per collision with the laser beam, and $\Gamma \simeq nAV$ is the rate of such collisions. For a thermal gas, V is the thermal velocity $V_T = \sqrt{2k_B T/M}$. We rewrite this as $V = \omega_z R_z$ and use this relation to obtain the velocity V for the condensate as $V_C = \sqrt{2}c_s$, where R_z is the Thomas-Fermi radius. This could also be derived from the pressure $nMc_s^2/2$ exerted by the condensate on the stirrer.¹⁶ Therefore, in comparing heating in a thermal cloud and a condensate we should assume that the condensate atoms strike the stirrer with a velocity $V_C \propto c_s$. The ratio r of the energy transferred per collision with the laser beam for normal and condensed gases is then

$$r = \frac{\Delta_T}{\Delta_C} = \frac{N_T \kappa_T}{N_C \kappa_C} \cdot \frac{n_C A_C V_C}{n_T A_T V_T} \approx \frac{\kappa_T R_T}{\kappa_C R_C} \quad (17)$$

where R_T and R_C are the transverse sizes of the normal and condensed components, respectively. We measured this ratio as $r \simeq 2$. Thus outside the superfluid regime, the difference in intrinsic heating for normal and superfluid components is seen to be quite small. Each collision with the stirrer transfers an energy of about Mv^2 to the gas, both in the thermal cloud and the condensate. Thus the observed difference between the heating coefficients κ_T and κ_C is mainly geometrical due to the different cloud sizes. Below the transition temperature the contribution to the heating from the thermal cloud is suppressed due to the larger size as well as by the high condensate fraction. Above T_c one can clearly isolate the heating mechanism due to the normal component.

In conclusion, we have studied dissipation induced by a macroscopic stirrer in a Bose gas below and above the BEC transition temperature. We present high sensitivity calorimetric measurements showing that the critical velocity is lower than suggested by earlier data.¹¹ Measurements on dilute

thermal clouds support a kinetic model of heating. This provides a first approximation to dissipation below the BEC transition temperature, whereas at higher density interactions between the condensate and normal gas will modify the nature of excitations.²⁸

ACKNOWLEDGMENTS

We thank A. P. Chikkatur and A. Görlitz for experimental assistance, and S. Rica for useful discussions. This research is supported by NSF, ONR, ARO, NASA, and the David and Lucile Packard Foundation.

REFERENCES

1. P. Nozières and D. Pines, *The Theory of Quantum Liquids*, Addison-Wesley, Redwood City, CA, (1990).
2. W. Ketterle, D. S. Durfee, and D. M. Stamper-Kurn, in *Bose-Einstein Condensation in Atomic Gases, Proceedings of the International School of Physics Enrico Fermi, Course CXL*, M. Inguscio, S. Stringari, and C. Wieman (eds.), IOS Press, Amsterdam (1999), pp. 67–176.
3. E. A. Cornell, J. R. Ensher, and C. E. Wieman, in *Bose-Einstein Condensation in Atomic Gases, Proceedings of the International School of Physics Enrico Fermi, Course CXL*, M. Inguscio, S. Stringari, and C. Wieman (eds.), IOS Press, Amsterdam (1999), pp. 15–66.
4. D. S. Jin, J. R. Ensher, M. R. Matthews, C. E. Wieman, and E. A. Cornell, *Phys. Rev. Lett.* **77**, 420 (1996).
5. M.-O. Mewes, M. R. Andrews, N. J. van Druten, D. M. Kurn, D. S. Durfee, C. G. Townsend, and W. Ketterle, *Phys. Rev. Lett.* **77**, 988 (1996).
6. M. R. Andrews, D. M. Kurn, H.-J. Miesner, D. S. Durfee, C. G. Townsend, S. Inouye, and W. Ketterle, *Phys. Rev. Lett.* **79**, 553 (1997).
7. M. R. Andrews, C. G. Townsend, H.-J. Miesner, D. S. Durfee, D. M. Kurn, and W. Ketterle, *Science* **275**, 637 (1997).
8. M. R. Matthews, B. P. Anderson, P. C. Haljan, D. S. Hall, C. E. Wieman, and E. A. Cornell, *Phys. Rev. Lett.* **83**, 2498 (1999).
9. K. W. Madison, F. Chevy, W. Wohlleben, and J. Dalibard, *Phys. Rev. Lett.* **84**, 806 (2000).
10. O. M. Maragò, S. A. Hopkins, J. Arlt, E. Hodby, G. Hechenblaikner, and C. J. Foot, *Phys. Rev. Lett.* **84**, 256 (2000).
11. C. Raman, M. Köhl, R. Onofrio, D. S. Durfee, C. E. Kuklewicz, Z. Hadzibabic, and W. Ketterle, *Phys. Rev. Lett.* **83**, 2502 (1999).
12. A. P. Chikkatur, A. Görlitz, D. M. Stamper-Kurn, S. Inouye, S. Gupta, and W. Ketterle, *Phys. Rev. Lett.* **85**, 483 (2000).
13. R. Onofrio, C. Raman, J. M. Vogels, J. Abo-Shaeer, A. P. Chikkatur, and W. Ketterle, *Phys. Rev. Lett.* **85**, 2228 (2000).
14. K. B. Davis, M.-O. Mewes, M. R. Andrews, N. J. van Druten, D. S. Durfee, D. M. Kurn, and W. Ketterle, *Phys. Rev. Lett.* **75**, 3969 (1995).
15. S. Giorgini, L. P. Pitaevskii, and S. Stringari, *J. Low Temp. Phys.* **109**, 309 (1997).
16. F. Dalfovo, S. Giorgini, L. P. Pitaevskii, and S. Stringari, *Rev. Mod. Phys.* **71**, 463 (1999).
17. T. Frisch, Y. Pomeau, and S. Rica, *Phys. Rev. Lett.* **69**, 1644 (1992).

18. B. Jackson, J. F. McCann, and C. S. Adams, *Phys. Rev. Lett.* **80**, 3903 (1998).
19. B. Jackson, J. F. McCann, and C. S. Adams, *Phys. Rev. A* **61**, 051603(R) (2000).
20. C. Nore, C. Huepe, and M. E. Brachet, *Phys. Rev. Lett.* **84**, 2191 (2000).
21. M. Crescimanno, C. G. Koay, R. Peterson, and R. Walsworth, preprint cond-mat/0001163; *Phys. Rev. A*, in print.
22. P. O. Fedichev and G. V. Shlyapnikov, preprint cond-mat/0004039.
23. J. S. Stieβberger and W. Zwerger, preprint cond-mat/0006419; *Phys. Rev. A*, in print.
24. T. Winiecki, B. Jackson, J. F. McCann, and C. S. Adams, preprint cond-mat/0004430.
25. C. Huepe and M.-E. Brachet, *C. R. Acad. Sci. Paris Serie II* **325**, 195 (1997).
26. T. Winiecki, J. F. McCann, and C. S. Adams, *Phys. Rev. Lett.* **82**, 5186 (1999).
27. R. P. Feynman, in *Progress in Low Temperature Physics*, C. Gorter (ed.), North-Holland, Amsterdam, (1955), Vol. 1, p. 17.
28. E. Zaremba, T. Nikuni, and A. Griffin, *J. Low Temp. Phys.* **116**, 277 (1999).